



HAL
open science

Finite discrete element framework for investigating the effect of temperature-dependent dynamic viscosity on hydraulic fracturing

Murad S. Abuaisha, David Eaton, Jeffrey Priest, Ron Wong

► **To cite this version:**

Murad S. Abuaisha, David Eaton, Jeffrey Priest, Ron Wong. Finite discrete element framework for investigating the effect of temperature-dependent dynamic viscosity on hydraulic fracturing. Micro-seismic Industry Consortium: Annual Research Report, Volume 7, 2016. hal-02461113

HAL Id: hal-02461113

<https://minesparis-psl.hal.science/hal-02461113>

Submitted on 3 Feb 2020

HAL is a multi-disciplinary open access archive for the deposit and dissemination of scientific research documents, whether they are published or not. The documents may come from teaching and research institutions in France or abroad, or from public or private research centers.

L'archive ouverte pluridisciplinaire **HAL**, est destinée au dépôt et à la diffusion de documents scientifiques de niveau recherche, publiés ou non, émanant des établissements d'enseignement et de recherche français ou étrangers, des laboratoires publics ou privés.

Chapter 4

Finite discrete element framework for investigating the effect of temperature-dependent dynamic viscosity on hydraulic fracturing

Murad AbuAisha^{a,b}, David Eaton^a, Jeffrey Priest^b and Ron Wong^b

^a Dept. of Geoscience, Univ. of Calgary, Calgary, AB, T2N 1N4, Canada. E: morad.77.2@hotmail.com

^b Dept. of Civil Engineering, Univ. of Calgary, Calgary, AB, T2N 1N4, Canada. [-10pt]

4.1 Summary

In this chapter we provide a Finite-Discrete Element Method (FDEM) framework with fluid diffusion to investigate the effect of viscosity-temperature change on Hydraulic Fracturing (HF). The FDEM alone has been discussed and utilized in previous works, i.e. (*Munjiza et al.*, 1995). Here we present the mechanism for implementing fluid diffusion and leakoff in the FDEM approach (FDEM-HF). The analytical solution of fluid-driven fractures suggested by *Savitski and Detournay* (2002) is recalled, and the effect of viscosity-temperature change on the fracturing process and regime is scrutinized. This work ends by using the previous frameworks to investigate a large scale HF test, where the effect of viscosity-temperature change on the fracturing threshold/breakdown, fracture radius, and fluid leakoff and diffusion into the rock matrix are presented.

4.2 Introduction

Fluid diffusion and fracture leakoff are implemented in the FDEM approach (FDEM-HF) by considering the existence of flow channels that coincide with the edges of the triangular elements in the initial mesh¹. The nodes of the triangular elements represent virtual reservoirs where fluid pressure and fluid mass are sequentially calculated. The apertures of the flow channels are assigned initial values (a_i) that correspond to the initial permeability of the porous medium (Fig. 1).

Figure 1 illustrates the concept of implementing fluid diffusion and leakoff in the FDEM application. Fluid is injected at node N and fluid pressure consequently increases due to a fluid compressibility law. Because of the created pressure gradients, fluid then flows to nodes (virtual reservoirs) through the flow channels. The model also accounts

¹For more information about the FDEM, the reader is advised to check the works of *Lisjak et al.* (2014; 2013)

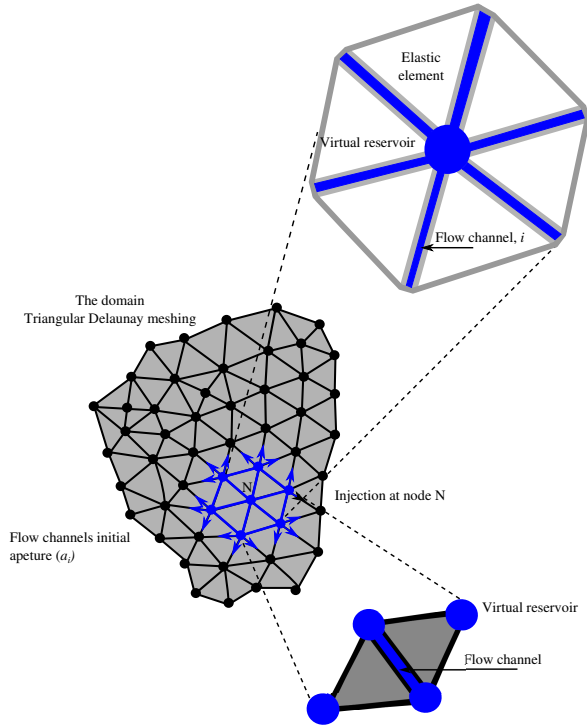


Figure 1 Conceptual graph that illustrates the implementation of fluid diffusion and leakoff in the FDEM approach (FDEM-HF). The flow takes place in flow channels that are initially assigned a finite aperture (a_i) which corresponds to the initial permeability of the medium. Each virtual reservoir, where fluid pressure is calculated, receives a mass of fluid from all branching channels.

for true/physical fluid cavities like boreholes. This new implementation of FDEM-HF has been detailed, tested, and verified in *Lisjak et al. (2017)*.

Based on the initial flow channel aperture (a_i), the initial volume of the virtual reservoir (V) is determined from the volume of conjunctive channels (Fig. 1) for a unity in the third dimension. The initial mass of fluid at each reservoir is calculated by adopting the same concept, yet the degree of saturation (S) is considered. Once the model starts undergoing the external loads and boundary conditions, the pressure and/or fluid masses at the virtual reservoirs change. Within a hydraulic time step i , the fluid pressure (p^i) at the virtual reservoirs is calculated while considering any increase/decrease of fluid mass (Δm) as well as any changes in the cavity volume itself,

$$p^i = \begin{cases} p^{i-1} + K_f \frac{\Delta m}{\rho_f V^i}, & \text{Change in fluid mass;} \\ p^{i-1} + K_f \frac{V^i - V^{i-1}}{(V^i - V^{i-1})/2}, & \text{in cavity volume;} \\ 0, & \text{for partially saturated media.} \end{cases} \quad (4.1)$$

K_f and ρ_f are the fluid bulk modulus and density respectively. The created pressure gradients between the virtual reservoirs incite fluid to flow in the channels. The fluid flow is assumed viscous and laminar, henceforth, it can be described using Darcy's law. The flow q between two reservoirs 1 and 2 within the time interval i of discretization Δt_h is described as,

$$q = \frac{\Delta m}{\Delta t_h} = f(S) \frac{p_1^i - p_2^i - \rho_f g(y_2 - y_1)}{R}, \quad (4.2)$$

with y_1 and y_2 being the elevations of the cavities/reservoirs 1 and 2 respectively. $f(S)$ is a dimensionless function that relates the permeability of the flow channel to the reservoirs degree of saturation. $f(S)$ ranges between 0 for perfectly dry reservoirs to 1 for fully saturated reservoirs. R is the flow resistance parameter of the channel that connects the reservoirs 1 and 2, and it is calculated using the cubic law for flow between two parallel plates (*Lisjak et al., 2017*),

$$R = 12 \eta \int_{l_1}^{l_2} \frac{1}{a(l)^3} dl = \frac{6\eta(a_1 + a_2)}{a_1^2 a_0^2} L, \quad (4.3)$$

where η is the fluid kinematic viscosity, L is the length of the flow channel, a_1 is the flow channel aperture at reservoir 1 and a_2 is the flow channel aperture at reservoir 2. The channel aperture is bounded between to limits for maximum opening and maximum closure beyond which further closing or opening have no meaning (*Lisjak et al., 2017*).

There are two distinct time discretizations in this approach of FDEM-HF. The first time scheme is used for the mechanical solver, i.e. deformation and fracturing. The second time scheme is used for the hydraulic solver, i.e. fluid diffusion and leakoff. The HM coupling is achieved by choosing the frequency between the mechanical and hydraulic solvers. For instance, the updates from the mechanical solver affect fluid pressure in the medium, and the resulting fluid pressure (from hydraulic solver) affect the mechanical calculations for the next time iteration. The stability of the hydraulic solver is assured by con-

trolling the size of the time step,

$$\Delta t_h \leq \min_m \left(\frac{V_m}{\frac{K_f}{\rho_f} \sum_n \frac{1}{R_n}} \right), \quad (4.4)$$

m and n index over all the cavities and flow channels in the boundary problem.

4.3 Water viscosity–temperature relation

Dynamic viscosity of a fluid describes its resistance to gradual deformation, and hence flow. It can be thought of as a measure of fluid friction. Water viscosity is independent of fluid pressure except for very high values larger than 80 MPa, yet it is strongly dependent on temperature (Likhachev, 2003). Viscosity of liquid water at different temperatures up to the normal boiling point is listed in Table (1)².

Table 1 Dynamic viscosity of water substance at different temperatures (1 cP(centipoise)= 10⁻³ Pa.s).

Temperature T (°C)	Dynamic viscosity μ (cP)
10	1.308
20	1.002
30	0.7978
40	0.6531
50	0.5471
60	0.4658
70	0.4044
80	0.3350
90	0.3150
100	0.2822

Burger *et al.* (1985) indicated that the variation of water substance viscosity in temperature range of 0 °C to 370 °C can be approximated by Eq. 4.5, T in Kelvin, with an accuracy of 97.5%.

$$\mu = 2.414 \times 10^{-5} \times 10^{\left(\frac{247.8}{T - 140}\right)} \quad (\text{Pa.s}) \quad (4.5)$$

Figure 1 shows a quite good agreement between the experimental record of Table (1) and the analytical expression of Burger *et al.* (1985) for the temperature range of 10 °C to 100 °C.

²www.engineeringtoolbox.com

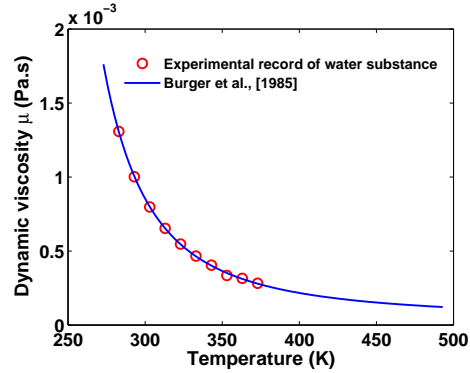


Figure 2 Correlation between the experimental record of the water substance shown in Table (1) and the analytical expression of Burger *et al.* (1985).

4.4 Fluid–driven fracture: Effect of fluid viscosity

This section presents an analysis of the propagation of a penny–shaped hydraulic fracture in an impermeable elastic rock. The fracture is driven by an incompressible Newtonian fluid injected from a source at the center of the fracture. The fluid flow is modelled according to lubrication theory, while the elastic response is governed by a singular integral equation relating the crack opening and the fluid pressure. It is shown that the scaled equations contain only one parameter, a dimensionless viscosity, which controls the regimes of fracture propagation. Asymptotic solutions for zero and large dimensionless viscosity are constructed.

4.4.1 Problem formulation and analytical solution

Consider an axisymmetric hydraulic fracture propagating in an infinite impermeable elastic medium characterized by Young’s modulus E , Poisson’s ratio ν , and toughness K_{Ic} (Fig. 2). An incompressible Newtonian fluid with viscosity μ is injected at the center of the fracture at constant volumetric rate Q_0 . We seek to determine the crack aperture $w(r, t)$ as a function of the radial coordinate r and time t , the net pressure $p(r, t)$ (the difference between the fluid pressure p_f and the far–field compressive stress σ_0 perpendicular to the fracture plane), and the fracture radius $R(t)$.

The analytical solution, in a toughness scaling, is obtained by scaling the set of equations and boundaries described in Savitski and Detournay (2002). To get the solution, first it is convenient to define a viscosity μ' and a toughness K' , respectively proportional to μ and K_{Ic} , to avoid carrying

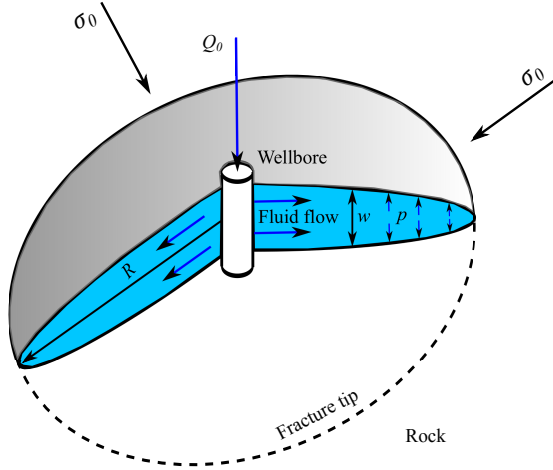


Figure 3 A penny-shaped hydraulic fracture: radial propagation, modified after *Savitski and Detournay (2002)*.

numerical factors in the equations,

$$\mu' = 12\mu, \quad K' = 4 \left(\frac{2}{\pi} \right)^2 K_{Ic}. \quad (4.6)$$

It is also natural to introduce the dimensionless toughness \mathcal{K} ,

$$\mathcal{K} = K' \left(\frac{t^2}{\mu'^5 Q_0^3 E'^{13}} \right)^{1/18}, \quad (4.7)$$

where $E' = E/(1-\nu^2)$. A dimensionless viscosity \mathcal{M} is logically defined as in *Savitski and Detournay (2002)* as well,

$$\mathcal{M} = \mu' \left(\frac{Q_0^3 E'^{13}}{K'^{18} t^2} \right)^{1/5}, \quad (4.8)$$

the dimensionless viscosity \mathcal{M} and toughness \mathcal{K} are simply related by,

$$\mathcal{M} = \mathcal{K}^{-18/5}. \quad (4.9)$$

We seek a solution of the form $\mathcal{F} = \{\Omega, \Pi, \gamma\}$ to order of the dimensionless viscosity \mathcal{M} , in the form of regular asymptotic expansion,

$$\mathcal{F}(\mathcal{M}) = \mathcal{F}_0 + \mathcal{M}\mathcal{F}_1 + O(\mathcal{M}^2), \quad (4.10)$$

where $\mathcal{F}_0 = \{\Omega_0, \Pi_0, \gamma_0\}$ and $\mathcal{F}_1 = \{\Omega_1, \Pi_1, \gamma_1\}$ are the zero and first order solutions of the dimensionless fracture aperture Ω , dimensionless fracture length γ , and dimensionless net pressure Π . The following sets of equations for the zero- and first-order terms are obtained:

- the zero-order solution, \mathcal{F}_0 , corresponds to an inviscid fluid ($\mathcal{M} = 0$) and is given in a closed form by

Savitski and Detournay (2002),

$$\begin{aligned} \Pi_0 &= \frac{\pi}{8} \left(\frac{\pi}{12} \right)^{1/5} \approx 0.3004; \\ \Omega_0 &= \left(\frac{3}{8\pi} \right)^{1/5} (1-\rho^2)^{1/2}; \\ \gamma_0 &= \left(\frac{3}{\pi\sqrt{2}} \right)^{2/5} \approx 0.8546; \end{aligned} \quad (4.11)$$

ρ ($0 \leq \rho \leq 1$) is the dimensionless fracture tip coordinate,

- the first-order, \mathcal{F}_1 , solution can also be expressed as in *Savitski and Detournay (2002)*,

$$\begin{aligned} \Pi_1 &= \Pi_1^* - A \left[\frac{1}{3} \ln \rho - \frac{1}{5} \ln(1-\rho^2) \right]; \\ \Omega_1 &= B(1-\rho^2)^{1/2} - \frac{8}{3\pi} A \gamma_0 \left[\left(\ln 2 - \frac{4}{5} \right) \times \right. \\ &\quad \left. (1-\rho^2)^{1/2} + \rho \cos^{-1} \rho - \frac{6}{5} I^*(\rho) \right]; \\ \gamma_1 &= -\frac{544}{75\pi^2} \approx -0.7349, \end{aligned} \quad (4.12)$$

where the constants $\Pi_1^* \approx 0.6380$, $A \approx 1.709$, and $B \approx 0.8264$. The function, $I^*(\rho)$, defined as,

$$I^*(\rho) = \int_{\rho}^1 \sqrt{\frac{1-\xi^2}{\xi^2-\rho^2}} \cos^{-1} \xi \, d\xi, \quad (4.13)$$

with ξ being the non-local integral operator, has to be evaluated numerically.

4.4.2 Effect of viscosity-temperature change

If fluid viscosity in Eq. 4.6 is updated due to different changes in the ambient temperature, the dimensionless viscosity \mathcal{M} will consequently change, i.e. $\mathcal{M} = f(t, \mu(T))$. For the rock properties and operating conditions in Farrell Creek Montney reservoir (Sect. 4.5); i.e. elastic modulus $E = 42.5$ MPa, Poisson's ration $\nu = 0.17$, injection rate $Q_0 = 5 \times 10^{-4}$ m³/s, and material toughness $K_{Ic} = 1.1$ MPa/m^{0.5}, the contours of the dimensionless viscosity (eq. 4.8) over a viscosity range of $[12 \text{ to } 4] \times 10^{-4}$ Pa.s, and corresponding to a temperature change of $[10 \text{ to } 80]$ °C (assuming substance water), is shown in Fig. 5.6(b).

Figure 5 shows the contours of the dimensionless pressure Π along the radial fracture over a viscosity range of $[12 \text{ to } 4] \times 10^{-4}$ Pa.s, and corresponding to a temperature change of $[10 \text{ to } 80]$ °C, and at two time steps of 10 and 45 s.

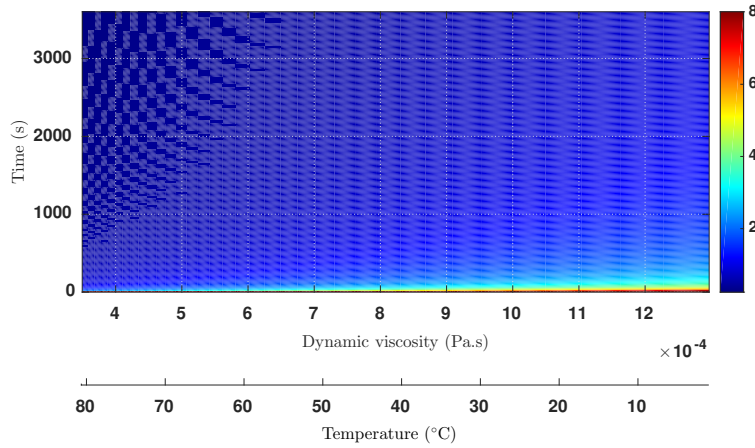


Figure 4 Contours of the dimensionless viscosity \mathcal{M} over a viscosity range of $[12 \text{ to } 4] \times 10^{-4}$ Pa.s, and corresponding to a temperature change of $[10 \text{ to } 80]$ °C. The time span of 3600 seconds, i.e. an injection test of 60 minutes.

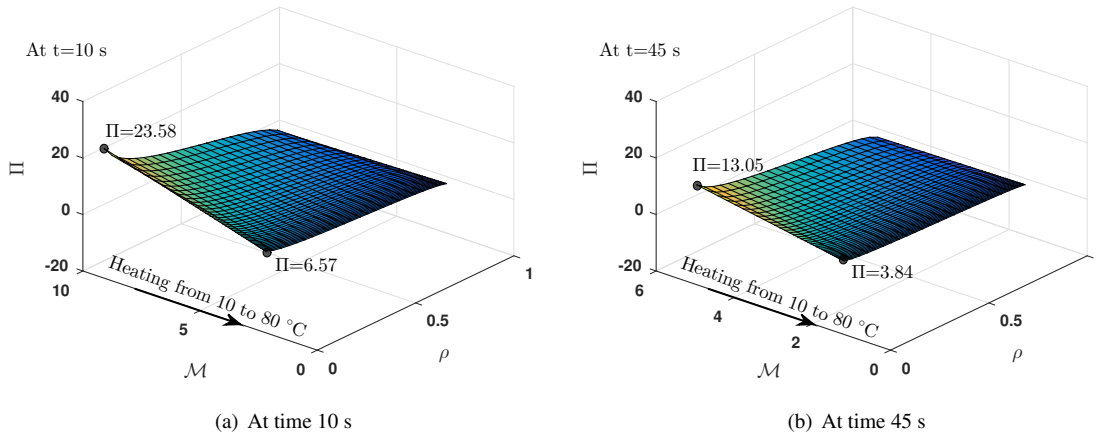


Figure 5 Contours of dimensionless pressure along the fracture dimensionless radius ρ , and for a viscosity range of $[12 \text{ to } 4] \times 10^{-4}$ Pa.s corresponding to a temperature change of $[10 \text{ to } 80]$ °C.

Following Fig. 5.6(b), it is observed that for such operating conditions and even at high temperatures of 80 °C, the fracturing will be viscosity dominated ($\mathcal{M} \geq 1$) even for a fracturing test of 60 minutes, same conclusions were reached by *Savitski and Detournay* (2002). Figure 5 indicates the fracturing net pressure is decreasing when increasing fluid temperature/decreasing fluid viscosity (transiting the fracturing system to toughness-dominated). The previous conclusion indicates that fracturing is more difficult when fluid temperature is high (fluid viscosity is low). The figure also demonstrates that the net fracturing pressure is decreasing with the operational time. This is due to the fact that as the fracture grows in length it becomes more difficult to drive it to grow more. It is that the fracturing system becomes less viscosity-dominated with the operational time. This re-

duction in the net fracturing pressure becomes less significant when the injected fluid is less viscous/more hot. For instance, and for injection time change from 10 s to 45 s, Π goes from 6.57 to 3.84 for low \mathcal{M} , however, it goes from 23.58 to 13.05 for high values of \mathcal{M} (Fig. 5).

4.5 Large scale HF test: Simulations and discussion

The Boundary Value Problem (BVP) uses a horizontal wellbore located in $200 \text{ m} \times 200 \text{ m}$ rock formation and drilled in the direction of minimum horizontal stress σ_h . The dimensions of the wellbore are neglected as the research focuses on large scale fracturing and fluid diffu-

sion. To capture the severe changes near the wellbore and to increase the outcome resolution, the mesh is intensively refined with 0.5 m elements in a area of 80 m \times 80 m. Away from the zone of the intensive refinement, element size is gradually increased to 3.0 m (Fig. 6).

The material properties pertaining to rock formation and needed in the numerical simulation are listed in Table (1). The input data as well as the *in situ* stress measurements correspond to Farrell Creek Montney reservoir of Total Vertica Depth TVD of 2099 m. The initial reservoir pressure is 34.84 MPa and far-field stresses are $\sigma_V = 53.1$ MPa and $\sigma_H = 44.2$ MPa.

Fluid is injected following two schemes: 1) at constant flow rate of 0.5 l/s, 2) at stepwise flow rate, where injection is constant (0.5 l/s) for the first 9.1 seconds and then injection is shut down and fluid is left to diffuse/seep through the porous medium. Each of the two schemes is run for tow different values of fluid viscosity, i.e. $\mu = 1 \times 10^{-3}$ Pa.s corresponding to $T = 20$ °C and $\mu = 0.5 \times 10^{-3}$ Pa.s corresponding to $T = 55$ °C.

Figure 7 shows the injected net fluid pressure profile for the two schemes of injection over a time span of ~ 45 seconds. Figure 8 shows the contours of the diffused fluid pressure and fracture patterns for the two schemes of injection and for the two possibilities of fluid viscosity. The contours of net fluid pressure and fracture patterns are plotted for different times corresponding to the letters (a to h) in Fig. 7. The letters (a to d) go for the case of viscosity $\mu = 1 \times 10^{-3}$ Pa.s, meanwhile the letters (e to h) go for $\mu = 0.5 \times 10^{-3}$ Pa.s (Fig. 8). The letters are picked up such that: 1) a and e correspond to a state in the fracture growing regime (after the fracturing threshold); 2) b and f at the shutdown time of 9.1 s; 3) c and j at the state of leakoff (after shut down and before diffusion in the medium); and 4) d and h somewhere in the middle of the diffusion process.

Following Fig. 7(a) and in either case of fluid viscosity, we can observe that fluid reaches a fracturing threshold before the pressure values drop to a constant value (11.3 MPa) of steady fracturing regime (this value is approximately equal to σ'_H). If the values of \mathcal{M} for the operating conditions of Table (1) and at time 45 s are calculated, one will get $\mathcal{M} = 3.98$ for $\mu = 1 \times 10^{-3}$ Pa.s and $\mathcal{M} = 1.99$ for $\mu = 0.5 \times 10^{-3}$ Pa.s. In both cases, and even at the end of the injection test, the values of \mathcal{M} are larger than 1.0, which indicates a viscosity dominated regime according to *Savitski and Detournay* (2002). Fluid pressure starts to increase after some time of continuous growing in the steady state. This is in agreement with the analytical solution of the penny-shaped fluid-driven fracture discussed previously. It is that after the fracture grows to a certain radius and after some time of injection, the value of \mathcal{M} gets smaller and consequently the dimensionless net pres-

sure Π (Fig. 5). This means that the fracturing regime becomes less viscosity-dominated and more pressure is needed to drive the bi-wing fracture to grow. One may think of this as it becomes more difficult to drive a bigger fracture to grow, i.e. more energy is needed. The previous conclusion is not observed in the pressure profile of $\mu = 0.5 \times 10^{-3}$ Pa.s, actually the steady state continues after the breakdown and for the entire injection period. This can be related to the fact that less viscous fluid tends to diffuse more and the net driving pressure is not significantly altered for lower values of \mathcal{M} /when the fracturing system becomes less viscosity-dominated (Fig. 5).

The instantaneous drop of the fluid pressure after shut-down in the case of $\mu = 1 \times 10^{-3}$ Pa.s is typically observed in the field fracturing tests. It can be justified by considering the lag between fluid front and fracture tip developed in any fluid-driven fracture. As soon as shutdown is applied, fractures stop growing and fluid fills up the lags which causes fluid pressure to drop. Subsequently, fluid starts to leakoff from the fracture surface (represented by the semi-horizontal line after shut-down of Fig. 7(b) before it starts to diffuse in the porous medium (represented by the parabolic behaviour of Fig. 7(b)). The pressure drop due to shutdown is not noted for the case of $\mu = 0.5 \times 10^{-3}$ Pa.s, this can be related to the fact that lags between fluid front and fracture tips are much smaller when the fluid is not so viscous (*Savitski and Detournay*, 2002). Alternatively, fluid starts leaking off after shutdown till point j, then it starts to diffuse in the medium following a parabolic behaviour yet much faster than $\mu = 1 \times 10^{-3}$ Pa.s.

Figure 8 shows that viscous working fluid create longer fractures, i.e. they are favourable for optimum fracturing.

4.6 Conclusion

It is observed that temperature change of 35 °, usually corresponding to 1 km depth, is sufficient to decrease water viscosity by 50%. This change of water viscosity can significantly alter the fracturing process. It will increase the breakdown pressure by ~ 2 MPa, and will considerably affect the generated fracture radius and fluid diffusion into the porous medium. We conclude that accounting for temperature change in HF tests is necessary for accurate prediction of produced fracture patterns and breakdown pressures/calculations of ambient stresses (*AbuAisha et al.*, 2016; *AbuAisha and Lorent*, 2016a;b).

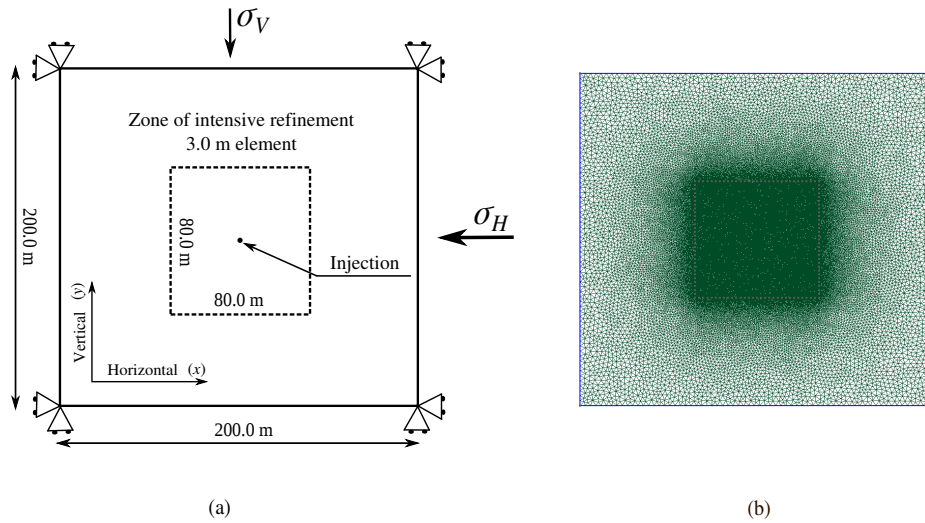


Figure 6 (a) The geometry and boundary conditions of BVP chosen for the HF simulations. The dimensions of the wellbore are neglected. (b) Triangular Delaunay meshing of the domain.

Table 2 Rock properties for a HF test of the BVP defined previously.

Nature	Parameter	Value	Unit
Elasticity	Drained Young's modulus, E	42.5	GPa
	Drained Poisson's ratio, ν	0.17	-
Fracture	Tensile strength, f_t	10.75	MPa
	Cohesion, c	21.1	MPa
	Mode I fracture energy, G_{Ic}	10	N/m
	Mode II fracture energy, G_{IIc}	100	N/m
	Material internal friction angle, ϕ_i	46.5	($^\circ$)
	Fracture friction angle, ϕ_f	46.5	($^\circ$)
Fluid flow	Dynamic viscosity, μ	1.0 or 0.5×10^{-3}	Pa.s
	Permeability, k	10^{-15}	m^2
	Biot's coefficient, κ	1.0	-
	Compressibility, K_f	2.2×10^9	MPa

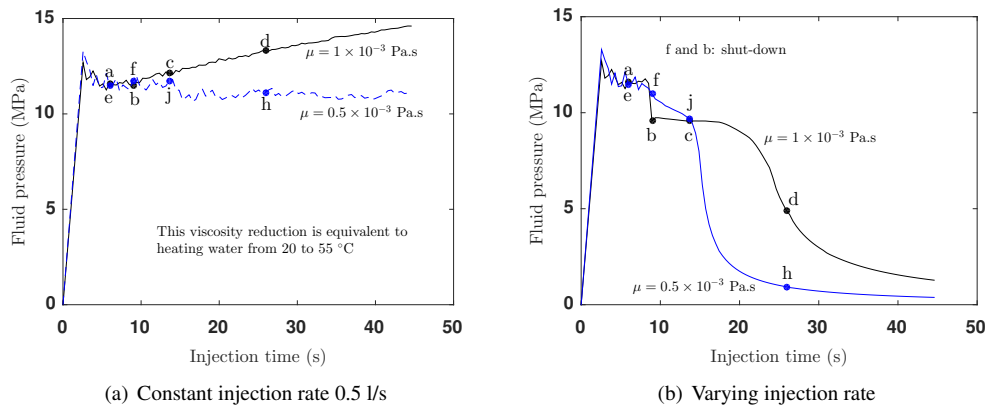


Figure 7 Net fluid pressure profile due to injection; a) at constant rate of 0.5 l/s, b) at constant rate of 0.5 l/s for the first 9.1 s and then shutting down.

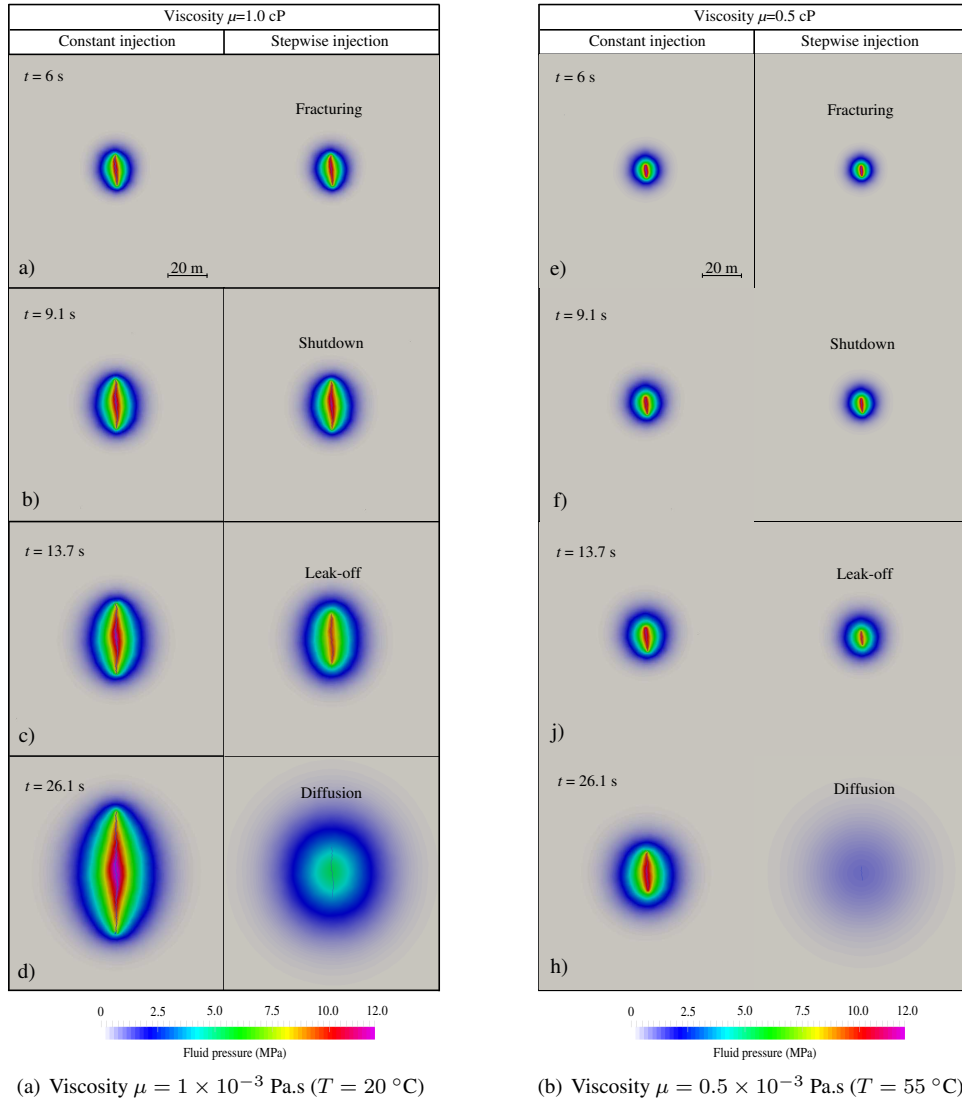


Figure 8 Fluid driven fracture patterns and diffused fluid pressure contours for the two schemes of injection and for two different values of fluid viscosity, i.e. $\mu = 1 \times 10^{-3}$ Pa.s corresponding to $T = 20$ °C and $\mu = 0.5 \times 10^{-3}$ Pa.s corresponding to $T = 55$ °C. These contours and fracture patterns are plotted for several injection times which correspond to the letters (a to h) in Fig. 7.

4.7 Acknowledgments

The author would like to thank the sponsors of the Microseismic Industry Consortium for financial support.

4.8 References

Munjiza, A., Owen, D. R. J., and Bicanic, N. A. (1995). A combined finite–discrete element method in transient dynamics of fracturing solids. *Engineering Computations* 12, 145–174.

Savitski, A., and Detournay, E. (2002). Propagation of a penny-shaped fluid-driven fracture in an impermeable rock: Asymptotic solutions. *International Journal of Solids and Structures* 39: 6311–6337.

Lisjak, A., Grasselli, G., and Vietor, T. (2014). Continuum–discontinuum analysis of failure mechanisms around unsupported circular excavations in anisotropic clay shales. *International Journal of Rock Mechanics and Mining Sciences* 65:96–115.

Lisjak, A., Liu, Q., Mahabadi, K. O., and Grasselli, G. (2013). Numerical simulation of acoustic emissions

- sion in brittle rocks by two-dimensional finite-discrete element analysis. *Geophysical Journal International* 195(1):423–443.
- Lisjak, A., Kaifosh, P., He, L., Tatone, B. S. A., Mahabadi, O. K., and Grasselli, G. (2017). A 2D, fully-coupled, hydro-mechanical, FDEM formulation for modelling fracturing processes in discontinuous, porous rock masses. *Computers and Geotechnics* 81, 1–18.
- Likhachev E. R. (2003). Dependence of water viscosity on temperature and pressure. *Technical Physics* 48(4):514–515.
- Burger, J., Sourieau, P., and Combarous, M. (1985). Thermal methods of oil recovery. Editions Technip, 45800 Saint-Jean-de-Braye.
- AbuAisha, M., Loret, B., and Eaton, D. (2016). Enhanced Geothermal Systems (EGS): Hydraulic fracturing in a thermo-poroelastic framework. *Journal of Petroleum Science and Engineering* 146, 1179–1191.
- AbuAisha, M., and Loret, B. (2016)a. Influence of hydraulic fracturing on impedance and efficiency of thermal recovery from HDR reservoirs. *Geomechanics for Energy and the Environment*, doi:10.1016/j.gete.2016.02.001.
- AbuAisha, M., and Loret, B. (2016)b. Stabilization of forced heat convection: Applications to Enhanced Geothermal Systems (EGS). *Transport in Porous Media* 112, 229–252.